The vesicular release probability sets the strength of individual Schaffer collateral synapses

Céline D. Dürst[1], J. Simon Wiegert[1,2], Christian Schulze[1], Nordine Helassa[3,4], Katalin Török[3] and Thomas G. Oertner[1]*

[1]Institute for Synaptic Physiology, Center for Molecular Neurobiology Hamburg (ZMNH), 20251 Hamburg, Germany

[2]Research Group Synaptic Wiring and Information Processing, Center for Molecular Neurobiology Hamburg (ZMNH), 20251 Hamburg, Germany

[3]Cell Biology and Genetics Research Centre, Molecular and Clinical Sciences Research Institute, St George's, University of London, London SW17 0RE, UK

[4]Department of Cardiovascular and Metabolic Medicine, Institute of Life Course and Medical Sciences, University of Liverpool, Liverpool, L69 3BX

*Correspondence: thomas.oertner@zmnh.uni-hamburg.de

Abstract

Information processing in the brain is controlled by quantal release of neurotransmitters, a tightly regulated process. Even in a single axon, presynaptic boutons differ in the number of docked vesicles, but it is not known if the vesicular release probability (p_{ves}) is homogenous or variable between individual boutons. We optically measured evoked transmitter release at individual Schaffer collateral synapses using the genetically encoded glutamate sensor iGluSnFR, localizing the fusion site on the bouton with high spatiotemporal precision. Fitting a binomial model to measured response amplitude distributions allowed us to extract the quantal parameters N, p_{ves}, and q. Schaffer collateral boutons typically released only a single vesicle under low p_{ves} conditions and switched to multivesicular release in high calcium saline. We found that p_{ves} was highly variable between individual boutons and had a dominant impact on presynaptic output.

Introduction

The conceptual framework of quantal synaptic transmission was developed at the frog neuromuscular junction (NMJ), a giant synapse containing thousands of transmitter vesicles [1]. Statistical analysis of electrophysiological recordings from innervated muscle cells suggested that neurotransmitter is released in multi-molecular packets ('quanta') which were later identified as synaptic vesicles. The strength of a specific NMJ could be mathematically described[2] as the product of the number of release sites N, their probability of release p_{ves}, and the postsynaptic response to the release of a single quantum, q. Applying quantal analysis to the very small synapses of the mammalian brain is not straightforward. In the brain, each neuron receives thousands of synapses, each of which has a different electrotonic distance from the postsynaptic cell body. Viewed from the soma, there is no unitary response: A single vesicle released at a distal dendritic synapse creates a much smaller EPSP than a vesicle released at a perisomatic synapse, making classical electrophysiological quantal analysis impossible. Attempts to electrically stimulate individual synapses gave rise to the hypothesis that individual synapses in the central nervous system can only release a single vesicle ('uniquantal release')[2]. With electrophysiology alone, however, it is difficult to distinguish between stimulation of multiple synapses and stimulation of a single synapse that is capable of multivesicular release.

Optical methods based on fluorescent calcium indicators have been used to resolve excitatory postsynaptic calcium transients (EPSCaTs) at individual synapses. Under conditions of high release probability, larger EPSCaTs were observed[3]. However, the amplitude of spine calcium transients depends on the local membrane potential in a highly non-linear fashion. The low number and stochastic behavior of postsynaptic NMDA receptors[4] adds variability to EPSCaTs, making it difficult to draw conclusions about vesicular release statistics from EPSCaT amplitude distributions. Furthermore, experimental manipulation of divalent ion concentration (Ca^{2+}, Mg^{2+}, Sr^{2+}) affect both the release machinery and the response of the optical calcium sensor, making the results of ion-substitution experiments difficult to interpret. In dissociated neuronal culture, it is possible to monitor vesicle fusion events using pH-sensitive green fluorescent proteins (pHluorins)[5,6]. A limitation of pH-based fusion detection is the lack of information about the filling state of the released vesicles[7].

Here we use the genetically encoded glutamate sensor iGluSnFR[8] to measure glutamate concentrations in the synaptic cleft[9,10]. We show that this probe is sensitive enough to detect the fusion of single vesicles at Schaffer collateral boutons in organotypic hippocampal cultures. At near-physiological calcium concentrations[11], synapses produced mostly failures and released single vesicles. Elevating the extracellular Ca^{2+} concentration caused synapses to increase their

release probability and to release multiple vesicles in response to single action potentials (APs). By localizing the fusion site on the surface of the presynaptic bouton with high precision, we show that multivesicular release occurs in a confined area, the active zone, which is stable over time. Using dual patch-clamp recordings and Monte Carlo simulations of glutamate diffusion, we show that the dynamic range of iGluSnFR is similar to postsynaptic AMPA receptors, although the kinetics of the underlying glutamate transients in the synaptic cleft is an order of magnitude faster. Thus, iGluSnFR signals are a good proxy for postsynaptic responses, but do not report the speed of glutamate diffusion out of the synaptic cleft. Comparing quantal parameters across boutons, we show that p_{ves} is the main determinant of synaptic strength under low release probability conditions, whereas *N* limits the strength of a given synapse under conditions of high release probability.

Results

We transfected individual CA3 pyramidal neurons in organotypic slices of rat hippocampus with iGluSnFR and the red fluorescent protein tdimer2 (Fig. 1a-b). Two to four days after transfection, we transferred the cultures to the recording chamber of a two-photon microscope (Extended Data Fig.1). As iGluSnFR is relatively dim in the absence of glutamate, we used the red cytoplasmic fluorescence to visualize soma, axons and boutons of transfected CA3 pyramidal cells (Fig. 1c-d). To evoke and measure release, we patch-clamped the transfected cells and triggered single APs by brief somatic current injections while imaging bouton fluorescence in CA1 *stratum radiatum* (Fig. 1e). Boutons belonging to the patched CA3 neuron were easily identified by a rapid increase in green fluorescence milliseconds after the somatically-triggered AP (Fig. 1f). Recording temperature was stabilized at 33 ± 1°C by Peltier-heating the oil immersion condenser.

The fast rise and decay kinetics of iGluSnFR[8,12] made it challenging to capture the peak of iGluSnFR fluorescence transients using the relatively slow raster scanning mode. Straight line scans across an individual bouton provide much better temporal resolution (up to 1 kHz), but are extremely sensitive to mechanical drift of the tissue: If the scan line misses the center of the rapidly diffusing cloud of glutamate, the true amplitude of individual release events will be underestimated. To capture the peak of the iGluSnFR signal, we modified ScanImage 3.8 [13] to allow user-defined spiral scans at 500 Hz, thus sampling the entire surface of the bouton every two milliseconds (Fig. 1g, *left*). As we did not know the exact location of the fusion site *a priori*, we did not use a static region of interest (ROI), but evaluated the spatial positions (columns in the time-space diagram) with the highest change in fluorescence (dynamic ROI, Fig. 1g). If no clear stimulus-evoked change in fluorescence was detected (potential failure trial), the same

columns as in the last trial were evaluated. In addition, we developed an automatic 3D repositioning routine to compensate for slow drift of the tissue, allowing stable optical recordings over hundreds of trials. To extract the amplitude of individual trials, we constructed a template (exponential decay) from several manually selected large responses. A single parameter (amplitude) was fit to match the template to each individual trial. Responses that exceeded 2σ of baseline fluctuations were classified as successes. Occasionally, we observed green fluorescent particles moving through the axon. Such events were detected by their elevated F_0 at baseline and excluded from further analysis (~2-5% of trials). At most boutons, the failure rate was stable over the time of the experiment (Fig. 1h). In principle, failure of glutamate release could be due to the stochastic nature of vesicle release or due to stochastic failures of AP propagation into individual branches of the extensive network of axon collaterals. In simultaneously imaged neighboring boutons, failures were not correlated, arguing for stochastic glutamate release (Fig. 1i).

Modulating synaptic release probability affects cleft glutamate concentration

Since presynaptic vesicle fusion is Ca^{2+}-dependent, we expected a steep dependence of the synaptic release probability p_{syn} on the extracellular Ca^{2+} concentration, $[Ca^{2+}]_e$. Indeed, switching $[Ca^{2+}]_e$ from 1 mM to 4 mM dramatically increased p_{syn} from 0.26 to 0.87 (Fig. 2a and b). Several boutons reached the ceiling of $p_{syn} = 1$ in 4 mM $[Ca^{2+}]_e$. Interestingly, the amplitude of iGluSnFR signals (successes) increased as well from 0.84 to 1.76 $\Delta F/F_0$ (Fig. 2b), indicating higher glutamate concentrations in the synaptic cleft under high p_{syn} conditions. In low $[Ca^{2+}]_e$, success amplitudes were similar across boutons (Fig. 2c). In high $[Ca^{2+}]_e$, however, the same set of boutons had variable success amplitudes that were strongly correlated with p_{syn}. To further explore the non-linear relationship between p_{syn} and cleft glutamate concentrations, we performed a set of experiments in 2 mM $[Ca^{2+}]_e$ (Fig. 2d). Under these conditions, p_{syn} was highly variable between individual boutons. Again, low p_{syn} boutons produced consistent success amplitudes (58% to 89% $\Delta F/F_0$ for $p_{syn} < 0.5$) while high p_{syn} boutons produced considerably larger successes. Boutons located next to each other on the same axon often had similar properties (Extended Data Fig. 2).

Taken together, these data indicate that p_{syn} is very variable between boutons and highly dependent on $[Ca^{2+}]_e$. Furthermore, as p_{syn} increased, so did the cleft glutamate, consistent with the capacity of Schaffer collateral boutons for multivesicular release[14–19].

Mapping the spatial location of individual fusion events

Large iGluSnFR signals from high p_{syn} boutons suggest multivesicular release, but are all vesicles released from a single active zone? To map the spatial location of individual release events (fusion site), we acquired rapid frame scans (16 × 16 pixels, 62.5 Hz) at high magnification (Fig. 3a). The red (cytoplasmic) fluorescence was used to align all frames *post hoc*. Putative vesicle fusion events were localized by fitting a two-dimensional Gaussian kernel to the green fluorescence in all success trials (Fig. 3b). We classified trials as successes or failures based on the standard deviation of fluorescence before stimulation (2σ criterion). In success trials, the putative fusion events were typically localized to a small region (Fig. 3c, 1 mM $[Ca^{2+}]_e$). Under conditions of increased release probability (Fig. 3c, 4 mM $[Ca^{2+}]_e$), fusion events remained localized to the same sub-region of the bouton. The same fitting procedure applied to failure trials resulted in a randomly distributed 'noise' map (Fig. 3c, failures), suggesting that the 2σ criterion correctly distinguished failures from successes. A similar random distribution was seen when the frame before stimulation was analyzed (Fig. 3c, baseline). The spatial distribution of fusion events was often elliptical, suggesting a synaptic contact on the side of the bouton (Fig. 3d). We fitted the distribution of the localized fusion events with an ellipse including 95% of the successes. We assume that the long axis of the fusion site distribution (range: 0.29 to 0.98 µm) represents the true diameter of the active zone whereas the short axis is the result of its geometrical projection. To calibrate our localization method, we acquired series of images from a green fluorescent microsphere next to a bouton, which resulted in more confined and circular maps (Fig. 3e). From these bead measurements, which were matched to the photon count of iGluSnFR signals, we estimate our localization precision to be 0.05 ± 0.01 µm, which is better than the lateral resolution of our microscope (0.48 ± 0.02 µm). In high $[Ca^{2+}]_e$, the same boutons displayed significantly more confined event distributions (Fig. 3f). In high $[Ca^{2+}]_e$, simultaneous fusion of multiple vesicles occurs frequently. Under these conditions, the glutamate cloud is not generated by a single 'point source', and we map the centroid of multiple fusion events. The distribution of centroids is expected to be less variable than the distribution of individual fusion events, explaining the tighter spatial distribution in high $[Ca^{2+}]_e$. Most importantly, the mapping experiments confirmed that at the majority of boutons, iGluSnFR signals were generated by a single active zone (Extended Data Fig. 3). In a few experiments, we found more than one active site on a single bouton (Extended Data Fig. 4). Such multi-synapse boutons, which could also be

identified in line scan mode, were excluded from further analysis. Taken together, our measurements show that synaptic vesicles are released at variable positions within a confined area (single active zone). Whether vesicle release sites were further organized into discrete nanodomains within the active zone, as has been shown for synapses grown on glass cover slips [6], could not be determined due to the intrinsic mechanical instability of brain tissue.

Desynchronized release events reveal quantal size

Although previous studies using postsynaptic measurements of AMPAR currents found evidence for multivesicular release at Schaffer collateral synapses[14,20], it has not been possible to compare the amplitude of evoked responses to the amplitude of spontaneous fusion events ('minis') *at the same synapse*. To perform a classical quantal analysis, the size of the quantum (q) has to be known. We therefore replaced extracellular Ca^{2+} with Sr^{2+} to desynchronize vesicle fusion events[21] while monitoring glutamate transients at single boutons (Fig. 4). Sr^{2+} is known to lead to asynchronous release due to its low affinity for synaptotagmin-1[22] and its slow clearance from the presynaptic terminal[23]. As expected, large-amplitude glutamate release events occurred with high probability in 4 mM $[Ca^{2+}]_e$. When artificial cerebrospinal fluid (ACSF) containing 4 mM Ca^{2+} was slowly replaced by ACSF containing 4 mM Sr^{2+}, evoked glutamate transients started to disintegrate into smaller events of relatively uniform amplitude. When 4 mM Sr^{2+} was fully washed-in, evoked responses completely disappeared while baseline fluorescence became very noisy. The amplitude histogram shows clear separation between evoked responses (Fig. 4b and c, blue bars) and delayed events (green bars). We interpret this sequence of events during wash-in as evoked multivesicular release, delayed release of individual vesicles under the influence of $[Sr^{2+}]_e$, and finally, incomplete fusion in the absence of $[Ca^{2+}]_e$. The quantal amplitude determined with this method was q = 96% ± 15% $\Delta F/F_0$ (n = 3 boutons).

The dynamic range of postsynaptic responses

Our optical measurements demonstrate a steep dependence of release probability on $[Ca^{2+}]_e$. Would AMPA receptors report increased glutamate concentrations as larger currents? To measure the strength of unitary connections, we performed dual patch-clamp recordings from connected pairs of CA3 and CA1 pyramidal cells under NMDAR block (10 µM CPP-ene) (Fig 5a). For each pair, we recorded EPSCs in 1 mM and in 4 mM $[Ca^{2+}]_e$, switching the sequence (low to high / high to low $[Ca^{2+}]_e$) between experiments. The boosting of AMPA EPSCs by high

$[Ca^{2+}]_e$ was similar to the boosting of iGluSnFR signals (Fig 5c), suggesting that AMPARs were able to transmit the very high transmitter concentrations reached in 4 mM $[Ca^{2+}]_e$ (Fig. 5e). Reducing AMPAR occupancy by the competitive antagonist γ-DGG (10 mM) did not increase the difference between low and high $[Ca^{2+}]_e$ EPSCs, suggesting that AMPARs were not saturated by stimulation in 4 mM $[Ca^{2+}]_e$ (Extended Data Fig. 5). We verified that blocking NMDARs did not affect the release of glutamate (Extended Data Fig. 6). Furthermore, in paired recordings, expression of iGluSnFR or a membrane-bound GFP in the postsynaptic cell did not change synaptic strength or paired-pulse ratio (Extended Data Fig. 7).

Due to vesicle pool depletion and AMPAR desensitization, we expected to see some degree of depression at higher stimulation frequencies, especially under conditions of high release probability (4 mM $[Ca^{2+}]_e$). We therefore compared the paired-pulse ratios from patch-clamp recordings of connected CA3-CA1 pairs and iGluSnFR signals from individual boutons. In 1 mM $[Ca^{2+}]_e$, EPSCs showed paired-pulse facilitation (PPR = 156%), which was absent in 4 mM $[Ca^{2+}]_e$ (PPR = 86%, Fig. 5b and f). iGluSnFR responses showed weak facilitation in 1 mM $[Ca^{2+}]_e$ (PPR = 110%) and depression in 4 mM $[Ca^{2+}]_e$ (PPR = 79%, Fig. 5d and f), consistent with the expected partial depletion of readily-releasable vesicles under high release probability conditions. We conclude that Schaffer collateral synapses are able to maintain a fairly linear paired pulse response over a ~10-fold change in synpatic strength, which is remarkable.

Non-linear response of iGluSnFR to glutamate release

Fusion of a single vesicle produces an extremely localized glutamate release into the synaptic cleft that rapidly disperses through diffusion. To explore how diffusing glutamate molecules, interact with iGluSnFR and postsynaptic AMPARs, we implemented a Monte Carlo simulation consisting of a glutamatergic bouton contacting a dendritic spine surrounded by astrocytes. Simulated fusion of a transmitter vesicle in the center of the synaptic cleft produced a local cloud of glutamate that filled the entire cleft within 10 µs and was largely cleared 100 µs later (Fig. 6a). Consequently, iGluSnFR molecules became bound (and fluorescent) and doubly bound AMPARs opened (Fig. 6b). The model allowed us to explore how different orientations of the synapse with respect to the optical axis would affect the amplitude of iGluSnFR signals (Fig. 6c and d). The largest signal in response to fusion of a single vesicle (quantal amplitude, q) is generated when both spine and axon are in the focal plane, aligning the synaptic cleft with the optical axis. A synapse where spine or axon are tilted with respect to the focal plane will produce smaller signals, since more extrasynaptic iGluSnFR molecules are inside the PSF and thus elevate the baseline fluorescence (F_0), decreasing the relative change in fluorescence ($\Delta F/F_0$).

This was an important insight, considering that a horizontal orientation of axons and spines is typical for organotypic slice cultures[24]. Nevertheless, we still expect variability in q between individual boutons due to variable spine orientations. Thus, when modeling iGluSnFR amplitude distributions, we treated q as a free parameter (search range: 50 – 200% $\Delta F/F_0$). The fraction of bright iGluSnFR and fraction of open AMPARs was low after release of a single vesicle (Fig. 6e), assuming 3000 molecules of glutamate per vesicle[25]. Simulated release of multiple vesicles increased the bound fraction of iGluSnFR and AMPARs. The saturation process was well approximated by hyperbolic functions

Equation 1: $$r = \frac{[\mathrm{Glu}]}{K_\mathrm{d} + [\mathrm{Glu}]}$$

where r corresponds to the fraction of iGluSnFR molecules (or AMPARs) bound to glutamate. Fraction of bound iGluSnFR and open AMPARs upon release of a single SV were 20% and 17%, respectively.

Extracting synaptic parameters by histogram analysis

The histograms of iGluSnFR responses from individual boutons often showed multiple peaks. Distinct quantal peaks have been observed in EPSC distributions from large mossy fiber synapses on CA3 pyramidal cells[26], but are much less clear at CA3-CA1 connections[27]. If these peaks indicate the simultaneous release of two or more vesicles in response to a single presynaptic AP, there are clear predictions about the amplitude and spacing of the peaks: The amplitude of the peaks would be expected to follow binomial statistics, as famously shown for endplate potentials[28]. Due to the saturation of iGluSnFR at 440% $\Delta F/F_0$, however, quantal peaks should not be equidistant, but compressed according to a hyperbolic saturation function (Equation 1).

To investigate release statistics in more detail, we performed optical quantal analysis from the iGluSnFR signals of individual Schaffer collateral boutons monitored 1 and 4 mM $[Ca^{2+}]_e$. The fluorescence trace in every trial was fit with a kernel (exponential decay function) to extract the peak amplitude. The resulting histograms were quite variable, sometimes displaying multiple peaks. To extract the three quantal parameters N, p_{ves}, and q from the response histograms, we generated predictions (probability density functions) for all possible parameter triplets (exhaustive search) to find the combination of parameters that explains best the histogram of iGluSnFR signals. First, for every combination of N and p_{ves}, we calculated the binomial probabilities for the different outcomes (failures, univesicular and various multivesicular events, Fig. 7a). From the baseline fluorescence distribution of the synapse in question, we extracted

the expected variability of failure fluorescence (width of the Gaussian). As photon shot noise increases with the square root of the number of detected photons, we added appropriate amounts of 'noise' to the expected quantal peaks leading to a broadening of the individual Gaussians as the signal increased. To account for partial saturation of iGluSnFR at high glutamate concentrations ((F_{max} - F_0) / F_0 = 440%, see methods), we spaced the expected quantal peaks not as integer multiples of q, but according to the saturation function (Equation 1). For every prediction, we scaled the amplitude to match the number of observations (histogram) and calculated the mean square error. We observed that different combinations of N and p_{ves} generated near-identical fits, as there was no 'cost' associated with increasing N in the model. We decided to select the prediction with the smallest number of vesicles that was within 2% of the minimum mean square error as the most parsimonious biophysical mechanism for the synapse in question. To further constrain the fitting procedure, the algorithm had to find values for q and for N that could account for the histogram of responses in 1 mM $[Ca^{2+}]_e$ and for the histogram count measured in 4 mM $[Ca^{2+}]_e$. The quantal size and number of release-ready vesicles are not expected to change with $[Ca^{2+}]_e$. Only p_{ves} was allowed to vary between the low and high $[Ca^{2+}]_e$ condition. The fitting results provided a convincing explanation why some boutons showed multiple peaks in 4 mM $[Ca^{2+}]_e$ while those multiple peaks were not apparent in 1 mM $[Ca^{2+}]_e$ (Fig. 7b and c, upper panels). Due to partial saturation of iGluSnFR at high glutamate concentration, quantal peaks for three or more simultaneously released vesicles are not resolved, but compressed into a broad peak (Fig. 7b and c, lower panels). In our sample of 27 boutons, the estimated number of docked vesicles ranged from 1 to 11, with only 2 boutons having just one docked vesicle. Changing $[Ca^{2+}]_e$ from 1 to 4 mM increased p_{ves} 9.9-fold (median change). A typical bouton in 1 mM $[Ca^{2+}]_e$ released a single vesicle in 20% of trials and multiple vesicles in only ~4% of trials. In 4 mM $[Ca^{2+}]_e$, multivesicular events were much more common (77%) and failures were rare (11%).

We estimated the iGluSnFR response to the release of a single vesicle (q) with three different approaches of increasing complexity: 1) by analyzing the amplitude of successes under low release probability conditions, 2) by measuring the amplitude of desynchronized events during $[Sr^{2+}]_e$ replacement experiments, and 3) by fitting a binomial model to the complete distribution of successes and failures from a single bouton (Fig. 7e). The resulting estimates of q were very consistent between methods and between individual experiments, indicating that the presynaptic *quantum* is indeed of constant size at glutamatergic synapses (although postsynaptic responses may vary). It is important to note that the absolute amplitude ($\Delta F/F_0$) of q depends not only on the indicator, but also on the spatial and temporal resolution of the microscope as it is trying to catch the peak fluorescence caused by a rapidly diffusing cloud of glutamate.

Vesicular release probability predicts synaptic strength in low Ca^{2+}

Lastly, we used our dataset to determine which synaptic parameter has the strongest impact on (pre-)synaptic strength. For each synapse, we calculated its synaptic strength as the product of quantal parameters ($p_{ves} \times N \times q$) under low and under high $[Ca^{2+}]_e$ conditions. Compared to simply averaging all iGluSnFR responses, this removes the compressive effect of indicator saturation. In 1 mM $[Ca^{2+}]_e$, p_{ves} was strongly correlated with synaptic strength p_{ves} ($R^2 = 0.663$, Fig. 8a), while the number of readily-releasable vesicles (N) showed almost no correlation ($R^2 = 0.018$). In 4 mM $[Ca^{2+}]_e$, however, the impact of N ($R^2 = 0.471$) was stronger than p_{ves} ($R^2 = 0.271$), suggesting that the number of readily-releasable vesicles limits the strength of a synapse under conditions of high release probability (Fig. 8b). In both conditions, quantal size q was not correlated with synaptic strength (Fig. 8a and b). As expected, synapses with low release probability showed pronounced paired-pulse facilitation ratio (Extended Data Fig. 8). The relation between p_{ves} and PPR followed a hyperbolic function[29].

In summary, most Schaffer collateral synapses are capable of increasing the glutamate output per AP under high release probability conditions and produce amplitude distributions consistent with binomial statistics. The vesicular release probability is remarkably variable between individual presynaptic terminals, suggesting that the distance between calcium channels and readily releasable vesicles is not uniform. Whether Schaffer collateral synapses operate in a high or low release probability regime when the animal is engaged in a behavioral task and when neuromodulatory inputs are active remains to be determined.

Discussion

Different approaches to optical quantal analysis

By measuring cleft glutamate transients at Schaffer collateral synapses under conditions of low and high release probability, we directly show the impressive dynamic range of individual boutons. The capacity for multivesicular release (MVR) has initially been inferred from the analysis of postsynaptic currents at various synapses in the CNS[20]. Optical approaches to quantal analysis were based on the analysis of spine Ca^{2+} transients (EPSCaTs) as a proxy for postsynaptic depolarization[18,30,31]. Compared to EPSCaT measurements, glutamate imaging has four distinct advantages: First, the unitary response to the release of a single vesicle (quantal size q, here measured in units of $\Delta F/F_0$) is determined by the properties of iGluSnFR and the resolution of the microscope and thus very similar across individual synapses. EPSCaT amplitude, in contrast, depends on the density of NMDARs, AMPARs, and the diluting volume of

the spine. The unitary EPSCaT is therefore different in every synapse, and it is practically impossible to wait for spontaneous EPSCaTs (the equivalent of “miniature end-plate potentials”) while imaging continuously. This is a serious drawback, as knowing *q* is at the heart of a true quantal analysis. Second, EPSCaTs are mediated by voltage-dependent NMDA receptors and voltage-gated calcium channels. Dendritic depolarization by other active synapses can therefore influence EPSCaT amplitude at the synapse under scrutiny. iGluSnFR signals, in contrast, are highly localized and unlikely to be contaminated by the activity of nearby synapses. Third, EPSCaTs are sensitive to the extracellular Ca^{2+} concentration while iGluSnFR is not. The calcium-independent read-out made it possible for us to directly investigate the impact of $[Ca^{2+}]_e$ on the release machinery and to replace Ca^{2+} by Sr^{2+}, generating desynchronized fusion events. Fourth, iGluSnFR directly probes the presynaptic function from a neuron of known identity. Several boutons on the same axon can be probed in parallel or sequentially, removing the bias towards strongly responding synapses that troubles EPSCaT analysis. Although other optical methods, such as styryl dyes or pHluorin-based indicators, share some of the advantages of iGluSnFR, they report vesicle fusion and not glutamate release. Therefore, indirect methods to sense the released glutamate have been used in the past. Electrical stimulation of single synapses and postsynaptic measurements of AMPAR currents has been widely used to estimate the quantal properties of synaptic transmission at glutamatergic synapses in many brain areas. However, this method depends on faithful translation of the synaptic glutamate concentration into AMPARs currents which is measured at the soma of the postsynaptic cell. Dendritic filtering and other electrotonic effects make this analysis challenging. Furthermore, bias may be introduced by the selection of stimulation conditions which yield all-or-none responses, discarding synapses with multi-quantal response characteristics.

The increase in synaptic glutamate associated with increased release probability observed in previous studies has been challenged by alternative explanations, namely diffusion of glutamate from adjacent sites[32]. Could the larger glutamate concentrations we observed under high release probability conditions be a result of synaptic spillover? In contrast to extracellular field stimulation which activates a large number of axons, we triggered APs in a single CA3 pyramidal cell. As presynaptic boutons on a single active axon are spatially well separated, spillover of glutamate is extremely unlikely. As a precaution, we performed all imaging experiments at 33°C to ensure efficient glutamate uptake by astrocytes. Furthermore, we observed the same local confinement of iGluSnFR transient under low and high release probability conditions, indicating that the source of glutamate was solely the active zone of the bouton under investigation.

Occupancy of glutamate sensors in the synaptic cleft

The steady-state glutamate affinity of iGluSnFR (K_d = 2.1 μM on neurons[12]) is similar to neuronal AMPARs (3–10 μM[33]). Glutamate concentrations are thought to reach 1.1 mM in hippocampal synapses[34], but AMPAR occupancy is nevertheless quite low[35]. As the glutamate transient in the synaptic cleft is very short[36], the *on*-rate rather than the steady-state affinity determines the occupancy after vesicular glutamate release. Our Monte-Carlo simulations suggest that the saturation curves of iGluSnFR and GluA1/GluA2 heteromers in the synaptic cleft are quite similar. Thus, iGluSnFR is a good proxy for the activation of postsynaptic receptors, but will not linearly report cleft glutamate. To extract quantal parameters from iGluSnFR signals, it is essential to correct for indicator non-linearity, as quantal peaks will not appear at integer multiples of *q*.

As iGluSnFR competes with excitatory amino acids transporters (EAATs) for glutamate, it slows down the clearance of bulk glutamate from the extracellular space[37]**.** However, diffusion of glutamate out of the synaptic cleft occurs at much shorter time scales (<100 μs) than uptake by EAATs. Our measurements of synaptic strength between pairs of connected CA3-CA1 neurons showed no significant difference between iGluSnFR-expressing and non-transfected CA3 neurons (Extended Data Fig. 7), demonstating that buffering effects of iGluSnFR did not affect postsynaptic AMPAR currents. The situation might be different for global expression of iGluSnFR or during periods of dense neuronal activity.

Quantal parameters and their variability

Our estimate of ~ 4 readily releasable SVs (median) is in line with other functional measurements based on statistic of synaptic transmission to quantify the number of release sites[18,38]. Electron tomography of glutamatergic synapses from rapidly frozen organotypic hippocampal slice cultures showed 10 to 12 docked vesicles per active zone[39]. Thus, not all docked vesicles might be release-competent. A recent study of primary hippocampal cultures determined the number of distinct release sites per active zone through a clustering method[5]. They estimated 10 release sites per active zone (assuming a release site diameter of 70 nm), but it is not clear whether all of these release sites are constantly occupied by release-ready vesicles. Another study on dissociated neurons, using total internal reflection fluorescence microscopy (TIRF) to monitor vesicle release with pHluorin, estimated 3 - 8 release sites per active zone[40]. Thus, while the absolute number of release-ready vesicles may vary with the

preparation and age of the culture[41], the range of 1-11 that we estimate from iGluSnFR analysis is consistent with estimates from other functional imaging approaches.

Quantal size, the iGluSnFR fluorescence change in response to the release of a single vesicle, was quite consitent between boutons (CV = 0.29), with amplitudes very similar to the desynchonized events we observed during Sr^{2+} wash-in. According to EM measurements of SV diameter, the mean vesicle volume varies between individual CA1 synapses up to five-fold (5000 nm^3 to 25000 nm^3) with a CV of 0.35[42,43]. Thus, it is possible that docked and release-ready vesicles are more consistent between synapses than the total pool of SVs. There is also variability of vesicle volume *within* boutons. Based on EM vesicle diameter measurements[42], the distribution of vesicle volumes is thought to be skewed with a CV = 0.38 (Ref. [44]). The fact that we and others[45] observed a pronounced gap in the iGluSnFR response histogram between single- and multivesicular events is not consistent with such a large variability. In our fitting procedure to determine the quantal parameters, we did not account for *any* variability in glutamate content. The only source of variability we included was photon shot noise, which we could precisely determine for every bouton from the fluctuations of baseline fluorescence. Including a term for quantal variability led to unrealistically broad distributions that were not compatible with the multi-peaked histograms we measured in high Ca^{2+}. Thus, it is possible that only vesicles with a specific diameter or filling state can dock and fuse, which would be a novel quality control mechanism ensuring quantal uniformity[7]. In summary, our functional measurements from live synapses suggest that glutamate quanta are more uniform than ultrastructural diameter measurements would suggest.

The relative importance of p_{ves} and N depends on the state of the synapse

Our results show that even the smallest synapses in the brain are capable of MVR. However, in 1 mM $[Ca^{2+}]_e$, which is close to physiological $[Ca^{2+}]_e$ in awake animals[11], p_{ves} is low (0.01-0.23) and MVR events are quite rare. We show that under these conditions, p_{ves} largely determines synaptic strength. Under high p_{syn} conditions, in contrast, N limits synaptic output. In vivo, the relative impact of p_{ves} and N on synaptic output may vary depending on the neuromodulatory state and the frequency of transmission. In our dataset, p_{ves} provided an excellent prediction of the paired-pulse ratio in 4 mM $[Ca^{2+}]_e$ (R^2 = 0.91, Extended Data Fig. 8), confirming previous studies[29,46]. Somewhat surprisingly, the number of release-ready vesicles showed no correlation with PPR, but the relatively long interval between the 2 pulses (ISI = 48 ms) might have been

sufficient to replenish vacant release sites. For sustained transmission at high frequencies, the number of release-ready vesicles might be rather critical[47,48].

Methods

Slice culture preparation. Organotypic hippocampal slices were prepared from Wistar rats P5-P7 as described previously[49]. Briefly, dissected hippocampi were cut into 400 µm slices with a tissue chopper and placed on a porous membrane (Millicell CM, Millipore). Cultures were maintained at 37°C, 5% CO_2 in a medium containing (for 500 ml): 394 ml Minimal Essential Medium (Sigma M7278), 100 ml heat inactivated donor horse serum (H1138 Sigma), 1 mM L-glutamine (Gibco 25030-024), 0.01 mg ml^{-1} insulin (Sigma I6634), 1.45 ml 5 M NaCl (S5150 Sigma), 2 mM $MgSO_4$ (Fluka 63126), 1.44 mM $CaCl_2$ (Fluka 21114), 0.00125% ascorbic acid (Fluka 11140), 13 mM D-glucose (Fluka 49152). No antibiotics were added to the culture medium. The medium was partially exchanged (60-70%) twice per week. Wistar rats were housed and bred at the University Medical Center Hamburg-Eppendorf (UKE). All procedures were performed in compliance with German law (Tierschutzgesetz der Bundesrepublik Deutschland, TierSchG) and according to the guidelines of Directive 2010/63/EU. Protocols were approved from the Behörde für Justiz und Verbraucherschutz (BJV) - Lebensmittelsicherheit und Veterinärwesen, Hamburg.

Plasmids and electroporation procedure. iGluSnFR, a gift from Loren Looger (Addgene plasmid #41732) and tdimer2, were each subcloned into a neuron-specific expression vector (pCI) under the control of the human synapsin1 promoter. Plasmids were diluted to 20 ng/µL and 40 ng/µL for tdimer2 and iGluSnFR, respectively, in K-gluconate-based solution consisting of (in mM): 135 K-gluconate, 4 $MgCl_2$, 4 Na_2-ATP, 0.4 Na-GTP, 10 Na_2-phosphocreatine, 3 ascorbate and 10 HEPES (pH 7.2). CA3 pyramidal neurons were transfected by single cell electroporation between DIV 17 and DIV 25 with a mixture of the two plasmids. During the electroporation procedure, slice cultures were maintained in pre-warmed HEPES-buffered solution consisting of (in mM): 145 NaCl, 10 HEPES, 25 D-glucose, 1 $MgCl_2$ and 2 $CaCl_2$ (pH 7.4, sterile filtered). An Axoporator 800A (Molecular Devices) was used to deliver 50 voltage pulses (-12 V, 0.5 ms) at 50 Hz[50].

Solutions and Electrophysiology. Experiments were performed 2 to 4 days after electroporation. Hippocampal slice cultures were placed in the recording chamber of the microscope and superfused with artificial cerebrospinal fluid (ACSF) containing (in mM): 127 NaCl, 25 $NaHCO_3$, 25 D-glucose, 1.25 NaH_2PO_4, 2.5 KCl, 2 $CaCl_2$, 1 $MgCl_2$. ACSF was

saturated with 95% O_2 and 5% CO_2. In the experiments where $[Ca^{2+}]_e$ was changed, we switched from 1 mM Ca^{2+}, 4 mM Mg^{2+} to 4 mM Ca^{2+}, 1 mM Mg^{2+} to keep the divalent ion concentration constant. Patch pipettes with a tip resistance of 3.5 to 4.5 MΩ were filled with (in mM): 135 K-gluconate, 4 $MgCl_2$, 4 Na_2-ATP, 0.4 Na-GTP, 10 Na_2-phosphocreatine, 3 ascorbate and 10 Hepes (pH 7.2). Experiments were performed at 33°C ± 1°C by controlling the temperature of the ACSF with an in-line heating system and the oil immersion condenser with a Peltier element. Whole-cell recordings from transfected CA3 pyramidal neurons were made with a Multiclamp 700B amplifier (Molecular Devices) under the control of Ephus software written in Matlab[51]. CA3 neurons were held in current clamp and stimulated through the patch pipette by brief electrical pulses (2-3 ms, 1.5-3.5 nA) to induce single APs. Individual trials (single pulse or paired-pulse) were delivered at a frequency of 0.1 Hz. The analog signals were filtered at 6 kHz and digitized at 10 kHz. For dual patch experiments, CA1 neurons were recorded in voltage clamp. Access resistance (R_{acc}) was monitored continuously throughout the experiment and recordings with R_{acc} > 20 MΩ were discarded. To isolate AMPA receptor responses, 10 µM CPP-ene was added to the perfusate.
For extracellular synaptic stimulation, a monopolar electrode was placed in *stratum radiatum* and two 0.2 ms pulses, 48 ms apart, were delivered using an ISO-Flex stimulator (A.M.P.I.). Stimulation intensity was adjusted to be subthreshold for APs. 10 mM γ-DGG was added to the bath in experiments were the fold change in AMPARs was probed under decrease of AMPARs saturation.

Two-photon microscopy. The custom-built two-photon imaging setup was based on an Olympus BX51WI microscope controlled by a customized version the open-source software package ScanImage[13] written in MATLAB (MathWorks). We used a pulsed Ti:Sapphire laser (MaiTai DeepSee, Spectra Physics) tuned to 980 nm to simultaneously excite both the cytoplasmic tdimer2 and the membrane bound iGluSnFR. Red and green fluorescence was detected through the objective (LUMPLFLN 60XW, 60×, 1.0 NA, Olympus) and through the oil immersion condenser (1.4 NA, Olympus) using 2 pairs of photomultiplier tubes (PMTs, H7422P-40SEL, Hamamatsu) (Extended Data Fig. 1), 560 DXCR dichroic mirrors and 525/50 and 607/70 emission filters (Chroma Technology) were used to separate green and red fluorescence. Excitation light was blocked by short-pass filters (ET700SP-2P, Chroma). ScanImage was modified to allow arbitrary line scanning. To measure iGluSnFR signals with a high signal-to-noise ratio, spiral scans were acquired to sample the surface of individual boutons. For single pulse stimulation, we acquired 44 spiral lines at 500 Hz or 330 Hz. For paired-pulse pulse

stimulation (48 ms ISI), we acquired 64 spiral lines at 500 Hz. Photomultiplier dark noise was measured before shutter opening and subtracted for every trial.

Drift Correction. To compensate for movements of the tissue during long imaging sessions, we developed an automated drift correction algorithm to re-center the synapse of interest. As spatial reference, we obtained a series of optical sections (z-step size: 0.5 µm) that were interpolated to 0.25 µm. For drift correction, we acquired a single frame-scan (test image) and performed subpixel image registration against the stack of reference images to extract lateral drift. In a second step, the overlapping regions from both, the test image and reference images were compared via cross correlation to reveal axial drift. Drift was compensated by adding offsets to the xy-scanner command voltages and by moving the objective to the correct z-position. Drift correction was typically completed within 0.3 s and performed before each stimulation trial.

Analysis of fluorescence transients. In case of a release event ('success'), a spiral scan covering the entire bouton may hit the diffusing cloud of glutamate just once or several times per line. We had no prior knowledge about the precise location of fusion events on the bouton surface. To maximize the signal-to-noise ratio in every trial, we assigned a dynamic region of interest (ROI): Pixel columns (i.e. spatial positions) were sorted according to the change in fluorescence (ΔF) in each column. In 'success' trials (average $\Delta F > 2\sigma$ of baseline noise), only columns which displayed a clear change in fluorescence ($\Delta F > ½$ max (ΔF)) were evaluated. In 'failure' trials (when ΔF of each column of the ROI was 5% > than ΔF of the corresponding columns in the baseline), the columns selected in the last 'success' trial were evaluated. At that stage, the classification used for ROI positioning (success vs. failure) was preliminary. Indeed, some 'failure' trials did show small fluorescent transients in the more sensitive ROI-based analysis. Boutons with a full width at half maximum (FWHM) of the amplitude distribution of the baseline (i.e. non-stimulated trials) larger than 0.4 were rejected as the imaging conditions were considered non-optimal and not considered for further analysis. To correct for bleaching, we fit an exponential decay to F_0 in failure trials. We corrected all data for bleaching by subtracting monoexponential fits acquired from the average fluorescence time course of failures. This bleach time constant was used to establish a photobleaching correction for each trial. To measure the amplitude iGluSnFR changes in fluorescence and to distinguish successful release of glutamate from failures, we used a template-based fitting algorithm. For each bouton we extracted a characteristic decay time constant by fitting a mono-exponential function to the average bleach-corrected iGluSnFR signals. To estimate the glutamate transient amplitude for every trial we kept the amplitude as the only free parameter. To check for overall stability, we

measured the mean F_0 (Baseline iGluSnFR signal) in each trial. If a trial had a $F_0 > 2\sigma$ measured out of the average F_0 of all trials then that trial was removed from the analysis.
The number of successes divided by the number of trials is the probability of release for a synapse (p_{syn}). We define the success amplitude to a single stimulus as the cleft glutamate ($[Glu]_{success}$).

Localization of release events. To map the position of fusion events on a bouton, we acquired 15 frames (16 × 16 pixels) at a rate of 62.5 Hz (16 ms per frame). Analysis of data consisted of four steps: de-noising, image alignment, estimating the amplitude of fluorescence transients, and localization of the release site. Raw images were first treated by a wavelet method to reduce photon shot noise[52]. Next, a cross talk correction was applied and the images were smoothed using a low pass filter (Gaussian kernel, 5 × 5 field size, $\sigma = 1$ pixel). Images were then up-sampled to 128 × 128 pixels (Lanczos3 kernel). For image alignment, we performed a Fast Fourier transform (FFT) on the red fluorescence signal (tdimer2). In addition, we used the red channel to define a continuous area encompassing bouton and axon (pixel intensity ≥ 10% to 30% of maximal intensity) as a morphology mask. The relative change in iGluSnFR fluorescence ($\Delta F/F_0$) was calculated using the mean of 5 baseline frames as F_0 (pixel by pixel). The top 3% of pixel values within the bouton mask were averaged to get the peak amplitude. All trials were tested for baseline stability which was defined as having overall highly similar images throughout the baseline frames (cross correlation ≥ 0.9). Trials not passing the threshold, for example when green fluorescent particles happened to pass through the bouton of interest, were excluded from further analysis.
To localize the fusion site, we constructed a template (2-D anisotropic Gaussian kernel) from the average of 5 ‘success’ trials. In the first round of analysis, we fit the template to every signal frame by adapting only the amplitude, keeping the location and shape of the kernel fixed at the template values. In trials where the release site is located not exactly at the template position, this procedure will underestimate the true amplitude. The goal of this first pass analysis was a preliminary classification of ‘successes’ ($\Delta F/F_0 > 2\sigma$ of baseline noise) and ‘failures’ ($\Delta F/F_0 < 2\sigma$ of baseline noise). To localize the fusion site in each individual trial, the fitting procedure was repeated, this time allowing for variable location. The location of the best fit corresponded to the most likely fusion site. This analysis was applied to all success trials, and a probability density function (2D Gaussian) was fitted to estimate the size of the active zone on the bouton. The same localization procedure was applied to the failure trials and, as a control, to a frame before stimulation. In most experiments, these two datasets produced random localizations, suggesting that our 2σ criterion was suitable to distinguish successes from failures. In cases where the

positions of apparent ‘failures’ clustered in a second area of the bouton, we classified this bouton as ‘multi-synapse bouton’ (Extended Data Fig. 4) and excluded it from further analysis.
To estimate the precision of our localization procedure, we imaged carboxylate-modified yellow-green fluorescent microbeads (0.17 µm diameter) positioned next to red fluorescent boutons and used the localization procedure described above to determine bead position relative to the bouton. As expected, localization precision was a function of the number of photons detected from the bead. At low laser power, we could match the bead intensity to the typical signal amplitude of iGluSnFR to the release of a single vesicle. Under these conditions, bead localization precision was 0.005 µm ± 0.01 µm.

Synapse modeling and glutamate release simulation. Release of glutamate and the time profile of iGluSnFR fluorescence were simulated using a Monte Carlo method (MCell) that considers the stochastic nature of molecule diffusion as well as that of reaction between molecules. The model consisted of an axon (diameter 0.2 µm, length 3 µm) with a varicosity representing the bouton (diameter 0.5 µm, length 0.5 µm), a hemispheric structure representing the spine (diameter 0.4 µm) attached to a cylindrical spine neck (diameter 0.2 µm). Active zone and postsynaptic density were defined as circular areas (diameter 300 nm) separated by the synaptic cleft (20 nm)[53]. Axon and spine were enclosed by an astrocytic compartment (width of extracellular space: 20 nm). Boundary conditions for the entire system were reflective. Glutamate transporters (GluT) were placed on astrocytic membranes at a density of 10.000 μm^{-2}. AMPARs were restricted to the PSD at a density of 1.200 μm^{-2} (resulting in ~85 receptors at a PSD diameter of 300 nm). Vesicle fusion was modeled by an instantaneous injection of glutamate at a fixed position (center of the active zone). The glutamate content of a single vesicle was estimated to be in the range of 2.000-3.000 molecules[25]. The diffusion coefficient of glutamate[54] was set to 200 $\mu m^2/s$. To study the consequences of univesicular and multivesicular release, we varied the number of released glutamate molecules between 3000 and 30.000 (1-10 vesicles).
Our model of iGluSnFR is based on a two-step reaction where rapid binding of glutamate to iGluSnFR is followed by a slower conformational change with concomitant increase in fluorescence:

$$\text{Glu} + \text{iGluSnFR} \underset{k_{-1}}{\overset{k_{+1}}{\rightleftharpoons}} \text{Glu-iGluSnFR}_{\text{dim}} \underset{k_{-2}}{\overset{k_{+2}}{\rightleftharpoons}} \text{Glu-iGluSnFR}_{\text{bright}} \qquad \text{(Equation 2)}$$

However, free glutamate dissipates from the synaptic cleft in ~100 µs, preventing equilibration of the first reaction. Therefore, the reaction can be linearized to

$$\text{Glu} + \text{iGluSnFR} \xrightarrow{k_{+1}} \text{Glu-iGluSnFR}_{\text{dim}} \xrightarrow{k_{+2}} \text{Glu-iGluSnFR}_{\text{bright}} \xrightarrow{k_{-2}} \text{Glu} + \text{iGluSnFR}_{\text{dim}} \quad \text{(Equation 3).}$$

Association and dissociation kinetics were measured *in vitro* revealing that the fluorescence change occurs in the second, isomerisation step[48]. Kinetic measurements of the conformational change of the purified protein gave k_{+2} of 569 s^{-1} and k_{-2} of 110 s^{-1} (ref. 48). The equivalent values from our cell-based measurements were 2481 s^{-1} and 111 s^{-1}, respectively (Extended Data Fig. 9). Such differences are expected between purified protein and cell-based measurements[8]. In addition to iGluSnFR, we included a kinetic AMPA receptor model[26] based on recordings (22 - 24°C) from rat hippocampal slices (age: p15 - p24). This model represents GluA1/GluA2 heteromers that are typical for CA3-CA1 synapses. We adjusted the rate constants to match the temperature of our experiments (33°C).

Quantal analysis. We wrote custom code (Matlab) to extract quantal parameters (https://github.com/toertner/optical-quantal-analysis). Analysis of optical signals is fundamentally different from EPSP analysis as the sources of noise are different and indicator saturation has to be considered. When collecting (green) fluorescence, the photon 'shot noise' follows Poisson statistics. For each bouton, we measured the standard deviation of baseline fluorescence (σ) in each trial before stimulation (baseline noise). Imaging conditions varied between individual experiments (depth in tissue, expression level, laser power) and we discarded experiments with baseline noise above 40%. For the remaining boutons, we generated predicted amplitude distributions based on binomial statistics. The width of the success distributions (Gaussians) was determined by the expected photon shot noise calculated from the baseline noise. Propagation of the shot noise was considered *in quadrature:*

$$\sigma Q = \sqrt{\sigma a^2 + \sigma a^2}$$

where a represents a probability density function for $N = 1$ and Q represents the propagated error. We explored the following parameter space: N: 1 to 15; p_{ves}: 0.1 to 0.99 (0.01 steps); q: 0.5 to 2.0 $\Delta F/F_0$ (0.01 steps).

Statistical Analysis. Normality was tested using D'Agostino-Pearson omnibus normality test. To test for significant differences between population means, Paired t test (two-sided) or the nonparametric Wilcoxon-Signed rank test. To compare independent populations, we used the unpaired t test (two-sided) or the nonparametric Mann–Whitney test as appropriate. Statistical significance was assumed when $p < 0.05$. Symbols used for assigning significance in figures: not significant (n.s.), $p > 0.05$; significant, $p < 0.05$(*), $p < 0.01$(**), and $p < 0.001$(***).

Acknowledgements

We thank Christine E. Gee and Mauro Pulin for critical reading of the manuscript and Iris Ohmert and Sabine Graf for slice culture preparation and excellent technical support. We thank Gary S. Bhumbra for helpful advice about quantal parameter extraction. This study was supported by the German Research Foundation DFG (SPP 1665 (to T.G.O); SPP 1926 (to J.S.W.); SFB 936 (to T.G.O.); FOR 2419 (to T.G.O. & J.S.W.)), Landesforschungsförderung Hamburg Z-FR LF (to T.G.O.), and BBSRC project grant BB/S003894/1 (to K.T.).

Author contributions

C.D.D., J.S.W., and T.G.O. designed the experiments. C.D.D. and T.G.O. prepared the manuscript. C.D.D. performed synaptic imaging experiments and analyzed the data. C.S. wrote software to acquire and analyzed GEGI data. N.H. and K.T. provided kinetic measurements of iGluSnFR. All authors read and approved the manuscript.

Competing financial interests

The authors declare no competing interest.

Data availability statement

Parameter files used for the MCell simulation have been deposited on GitHub (https://github.com/toertner/iGluSnFR-simulation). Imaging data are available from the corresponding author upon request.

Figures

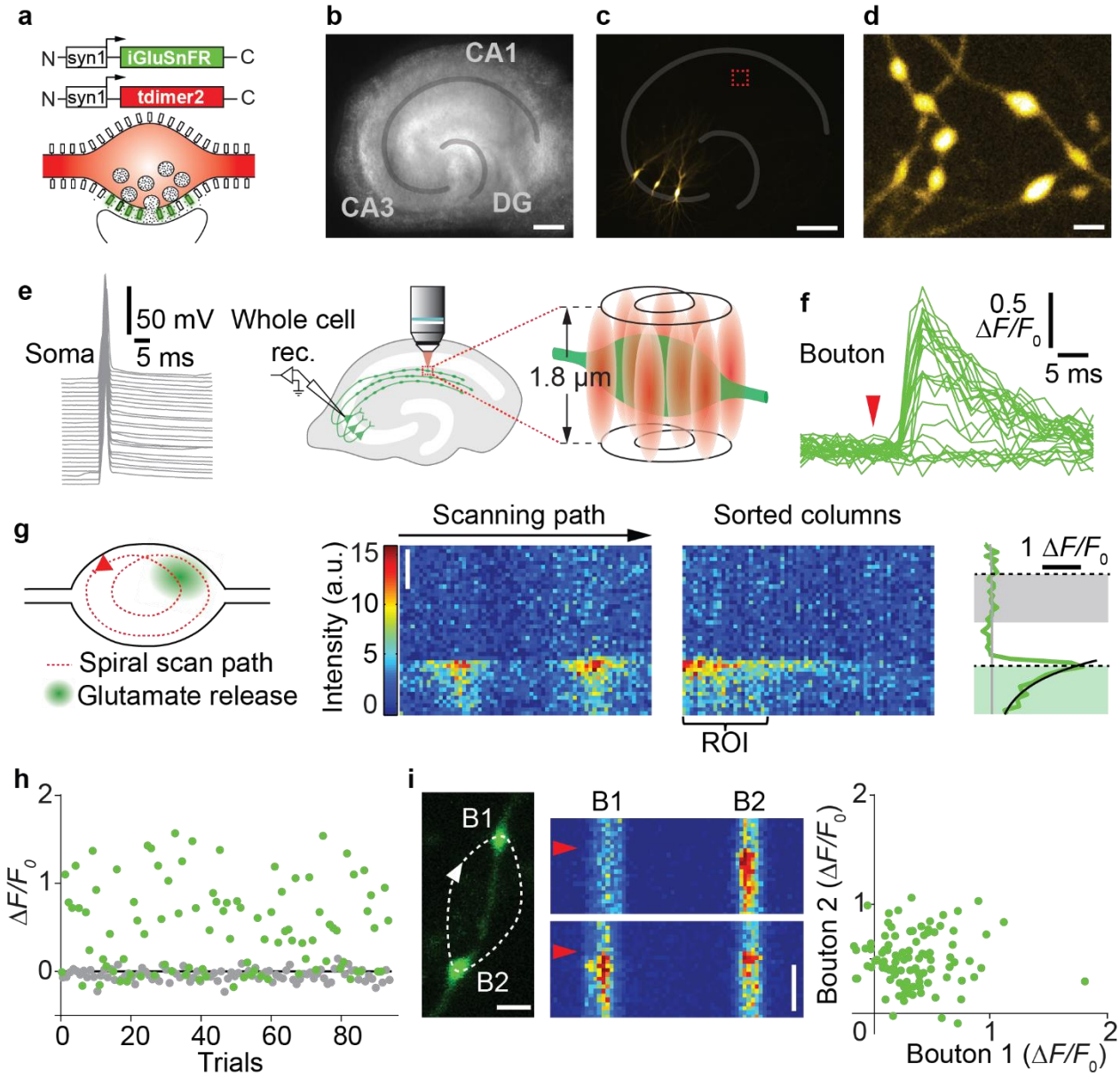

Figure 1: **iGluSnFR expression in CA3 pyramidal cells of organotypic slice culture of rat hippocampus. a)** *En passant* bouton co-expressing the cytoplasmic red fluorescent protein tdimer2 and green iGluSnFR exposed to the extracellular space. **b)** Transmitted light image of transfected organotypic hippocampal culture. Scale bar, 500 µm. **c)** Fluorescence image of three transfected CA3 neurons. Area for synaptic imaging is indicated (dotted box). Scale bar, 500 µm. **d)** Maximum intensity projection of a two-photon image stack of CA3 axons and their *en passant* boutons co-expressing tdimer2 and iGluSnFR in CA1 *stratum radiatum*. Scale bar, 1 µm. **e)** APs were reliably elicited in a transfected neuron by somatic current injections while glutamate release was simultaneously imaged from a single Schaffer collateral bouton in CA1. Owing to

the elongated point-spread function (PSF; red oval objects), the upper and lower surface of a bouton were simultaneously sampled by 500 Hz spiral scanning. **f)** Optical recording (iGluSnFR fluorescence) from a single Schaffer collateral bouton in CA1, showing a broad distribution of amplitudes and occasional failures. Red arrowhead indicates somatic current injection in CA3. **g)** Release events were typically sampled twice during every spiral scan. Fluorescence intensity (single trial) coded in rainbow colors. At t = 58 ms, a glutamate release event occurred. Scale bar, 20 ms. Only columns with $\Delta F > ½$ max (ΔF) were analyzed (dynamic region-of-interest). Response amplitude was estimated by exponential fit (green area, black fit) normalized by the resting fluorescence of the bouton (gray area, grey fit). The intersection between the horizontal black dashed lines and the fits corresponds to the extracted amplitudes (average peak amplitude for each experiment). **h)** Response amplitude (green circles) was constant over time. A time window before stimulation was analyzed to estimate imaging noise (gray circles). Response amplitudes were monitored in ACSF containing 2 mM $[Ca^{2+}]_e$ at 33°C. **i)** Monitoring two neighboring boutons located on the same axon. Scale bar, 1 µm. Two trials showing independent release events. Red arrowhead indicates the stimulation onset. Scale bar, 20 ms. iGluSnFR transients between neighboring boutons were not correlated ($R^2 < 0.0005$).

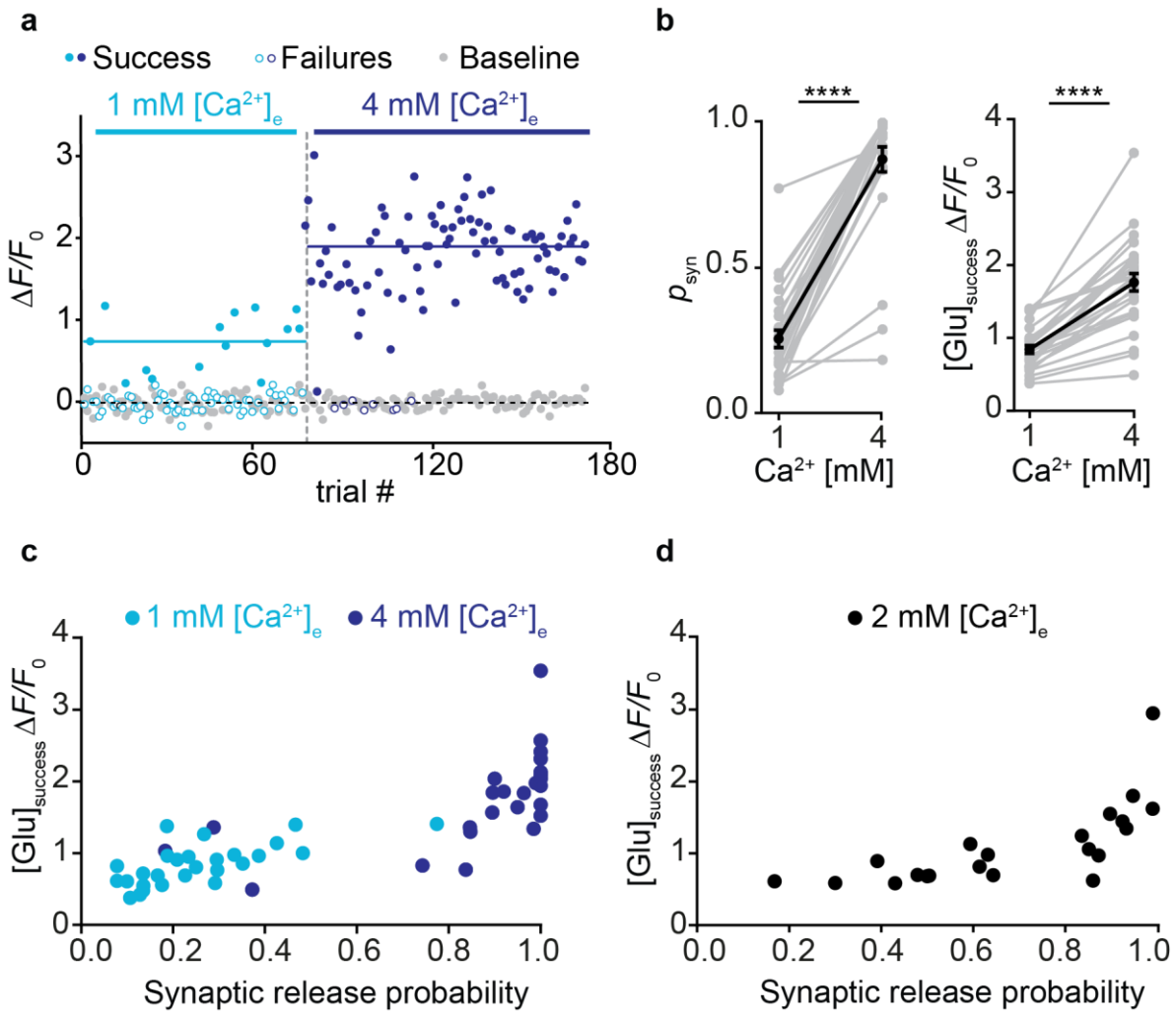

Figure 2: **Increasing release probability increases the glutamate concentration of synaptic transmission events. a)** Glutamate transients in a single bouton, switching from ACSF containing 1 mM $[Ca^{2+}]_e$ to 4 mM $[Ca^{2+}]_e$. The light blue and the dark blue lines represent the average of the amplitude of successes in 1 mM $[Ca^{2+}]_e$ and 4 mM $[Ca^{2+}]_e$ respectively. **b)** Summary of all experiments in 1 mM/4mM $[Ca^{2+}]_e$. The probability of successful glutamate release (*left panel*) increased from 0.26 ± 0.03 in 1 mM $[Ca^{2+}]_e$ to 0.87 ± 0.04 in 4 mM $[Ca^{2+}]_e$ (Wilcoxon signed rank test, $p < 0.0001$, $n = 27$ boutons in 23 slices). The amplitude of fluorescence transients in trials classified as 'success' (*right panel*) increased from 0.84 ± 0.056 $\Delta F/F_0$ in 1 mM $[Ca^{2+}]_e$ to 1.76 ± 0.12 $\Delta F/F_0$ in 4 mM $[Ca^{2+}]_e$ (paired t test, $p < 0.0001$, $n = 27$ boutons in 23 slices) indicating higher glutamate concentrations in the synaptic cleft under conditions of higher release probability. Values are given as mean ± SEM. **c)** The probability of successes was correlated with the amplitude of success trials in a non-linear fashion. **d)** In 2 mM $[Ca^{2+}]_e$, the synaptic release probability of individual synapses ranged from 0.17 to 0.99. The

amplitude of success trials was similar for boutons with low synaptic release probability but rose steeply for p_{syn} > 0.8.

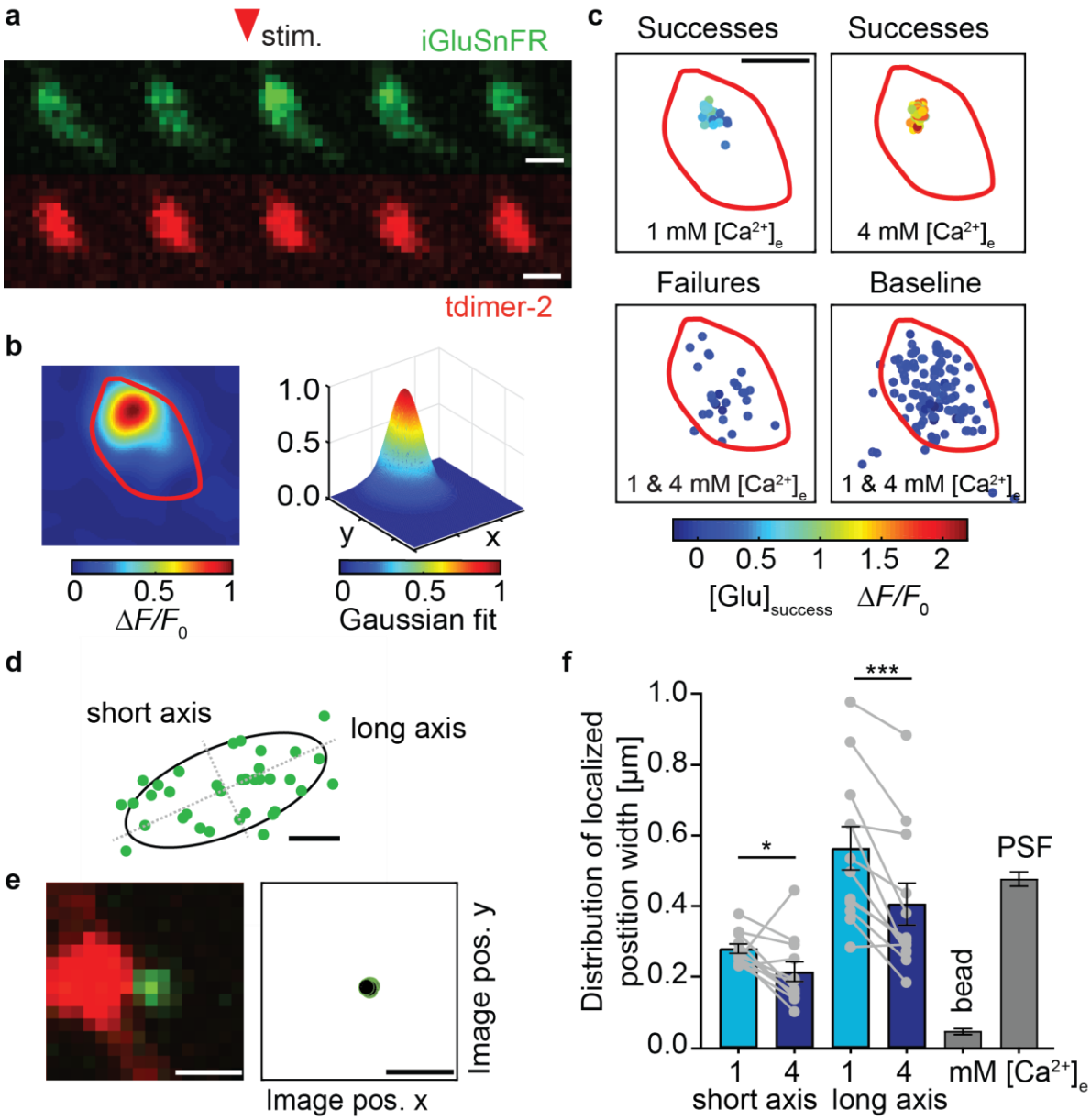

Figure 3**: Localizing the fusion site. a)** Time-lapse (frame rate 62.5 Hz) of a bouton releasing glutamate in response to an individual AP. Scale bar, 1 µm. **b)** (*Left*) top view of average responses of signals classified as successes. (*Right*) side view of the resulting 2D-Gaussian kernel fits. **c)** (*Upper left*) center positions of 2D-Gaussian kernel fits in success trials in ACSF containing 1 mM $[Ca^{2+}]_e$. (*Upper right*) center positions of 2D-Gaussian kernel fit in success trials in ACSF containing 4 mM $[Ca^{2+}]_e$. (*Lower left*) center positions of 2D-Gaussian kernel fits in failure trials (below 2σ of the baseline). (*Lower right*) center positions of 2D-Gaussian kernel fits in failure frames before the stimulation in ACSF containing 1 mM $[Ca^{2+}]_e$ and ACSF containing 4

mM $[Ca^{2+}]_e$. Scale bar, 1 µm. **d)** Example of a fitted ellipse including 95% of localized successes (green dots) from a single bouton. The length of the short and long axis of the fitted ellipse of successes measured in 1 mM $[Ca^{2+}]_e$ and 4 mM $[Ca^{2+}]_e$ are used to test for a relative enlarging of the release area in 4 mM $[Ca^{2+}]_e$ indicative of a multisynapse bouton. Scale bar, 128 nm. **e)** (*Left*) single plane of a two-photon microscope image of a bouton (tdimer2) next to a yellow-green fluorescent microspheric bead (0.17 µm). (*Right*) center positions of 2D-Gaussian kernel fits to the fluorescent signal of a bead. 50 consecutive images were acquired at 62.5 Hz. Scale bars, 1 µm. **f)** Histogram of short and long axis of the fitted ellipse to the localized responses and FWHM distribution of the localized bead and PSF measurement. Success localization short axis, 0.28 ± 0.01 µm in 1 mM $[Ca^{2+}]_e$ and 0.21 ± 0.03 µm in 4 mM $[Ca^{2+}]_e$ (Wilcoxon test, $p = 0.04$, $n = 12$ boutons); success localization long axis, 0.56 ± 0.06 µm in 1 mM $[Ca^{2+}]_e$ and 0.41 ± 0.06 µm in 4 mM $[Ca^{2+}]_e$ (Wilcoxon test, $p = 0.001$, $n = 12$ boutons); bead localization 0.05 ± 0.01 µm; PSF bead, 0.48 ± 0.02 µm). Values are given as mean ± SEM.

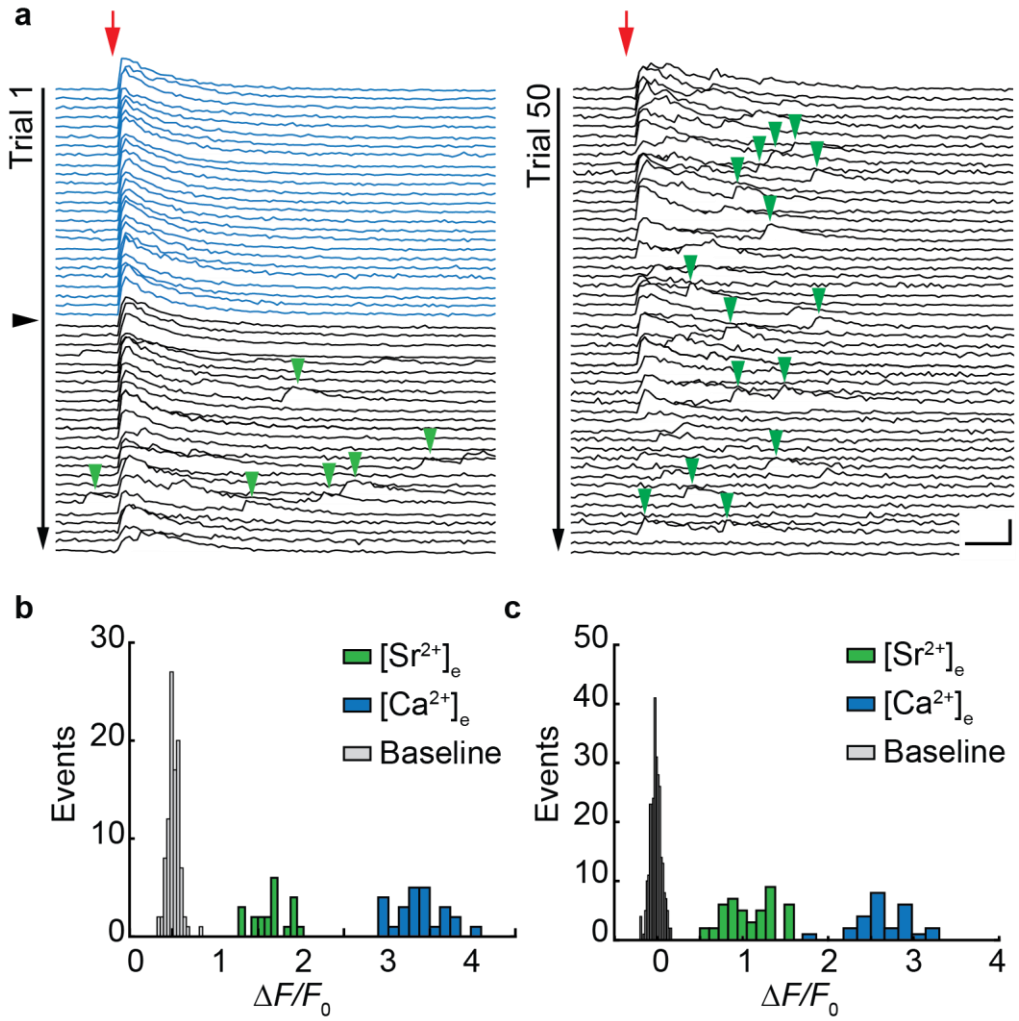

Figure 4: **Desynchronized release events reveal quantal size. a)** iGluSnFR changes in fluorescence (single bouton) in response to single APs in ACSF containing 4 mM $[Ca^{2+}]_e$ (blue traces). Red arrow indicates stimulation onset. Synaptic release probability was 1 (no failures). The black arrowhead indicates the start of 4 mM $[Sr^{2+}]_e$. wash-in. During wash-in of 4 mM $[Sr^{2+}]_e$ discrete events appear in the wake of the stimulation (green arrowheads). Scale bar, 2 $\Delta F/F_0$ and 20 ms. **b)** Amplitude histogram of evoked responses measured in 4 mM $[Ca^{2+}]_e$ (blue bars) and delayed events measured in 4 mM $[Sr^{2+}]_e$ (green bars) and fluctuation of baseline fluorescence (gray bars) of the example shown in (**a**). **c)** Amplitude histograms of a bouton with evoked responses measured in 4 mM $[Ca^{2+}]_e$ (blue bars), delayed events measured in 4 mM $[Sr^{2+}]_e$ (green bars) and fluctuation of baseline fluorescence (gray bars). The bin size is smaller for the baseline fluctuations for display purposes.

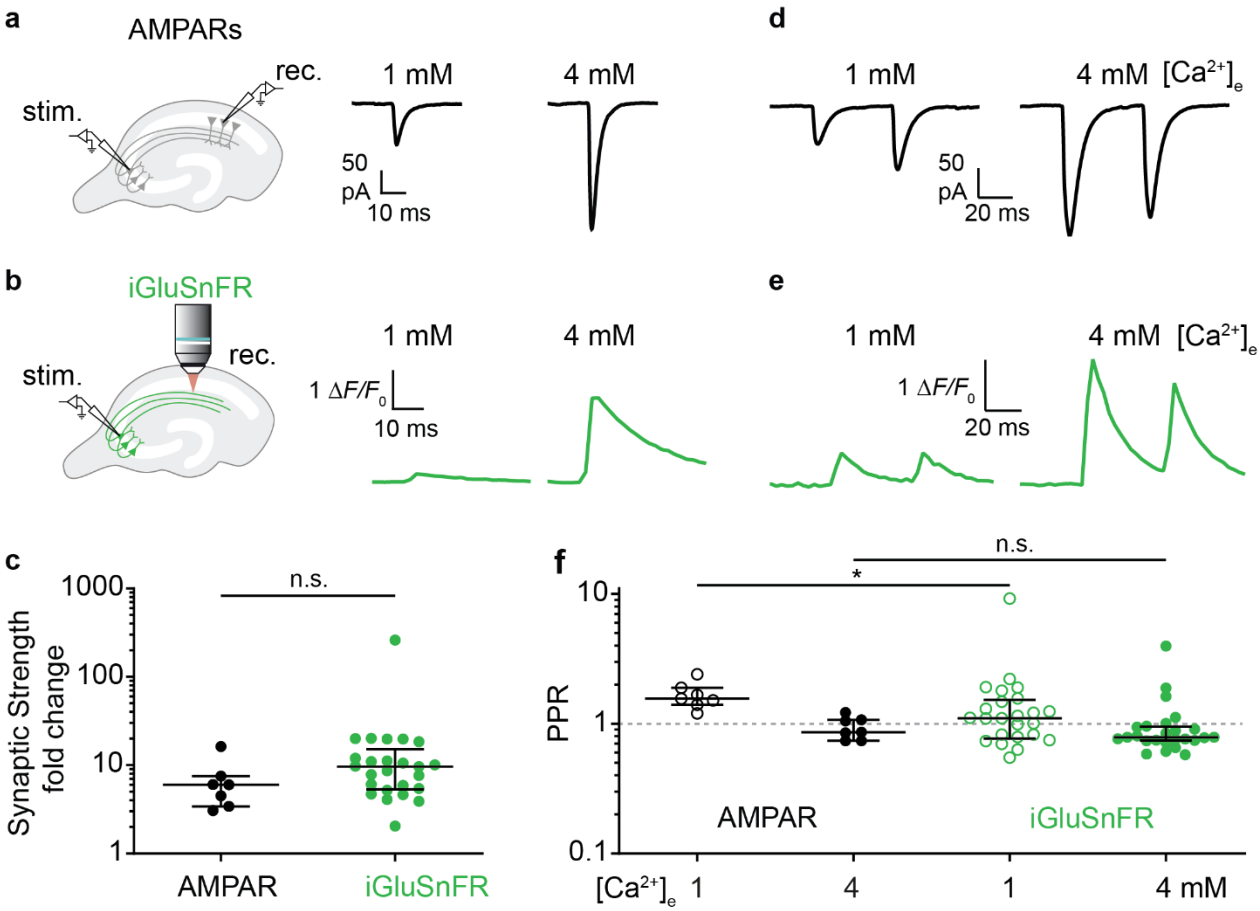

Figure 5: **Multivesicular release increases the gain and the signal to noise ratio of synapses. a)** EPSCs were measured by dual patch-clamp recordings from connected CA3-CA1 pyramidal cell pairs. Perfusion was switched from 1 mM to 4 mM $[Ca^{2+}]_e$, leading to increased EPSC amplitudes. Traces show EPSCs (average of ~40 trials) from the CA1 pyramidal cell. **b)** Representative EPSCs (average of ~40 trials) in response to the presynaptic paired-pulse stimulation (ISI 48 ms) recorded in 1 mM and 4 mM $[Ca^{2+}]_e$. **c)** iGluSnFR signals were measured as described previously (Fig. 1). Traces show the evoked change in fluorescence (average of ~60 trials) from a single bouton in CA1 stratum radiatum. The switching sequence (low - high $[Ca^{2+}]_e$ / high - low $[Ca^{2+}]_e$) was reversed between experiments. **d)** Representative iGluSnFR signals (average of ~60 trials) from a single bouton in CA1 *stratum radiatum* in response to the paired-pulse stimulation. **e)** Increasing $[Ca^{2+}]_e$ from 1 to 4 mM increased the median amplitude of AMPAR-mediated EPSCs by a factor of 6.02, interquartile range (IQR): 3.4–7.5 fold, n = 7 pairs, the median iGluSnFR response by 9.63 fold, IQR: 5.3 –15.2 fold, n = 25 boutons. There is no significant difference between the fold change in AMPARs and iGluSnFR responses (Mann-Whitney, p = 0.0832). **f)** EPSCs showed paired-pulse facilitation in 1 mM $[Ca^{2+}]_e$, (median PPR: 156%, IQR: 1.4%–1.9%, n = 7 pairs) and paired-pulse depression in 4 mM $[Ca^{2+}]_e$ (median PPR:

86%, IQR: 74%–107%, *n* = 7 pairs). iGluSnFR responses showed paired-pulse facilitation in 1 mM $[Ca^{2+}]_e$ (median PPR: 110%, IQR: 77%–152%, *n* = 25 boutons) and paired-pulse depression in 4 mM $[Ca^{2+}]_e$ (median PPR: 79%, IQR: 74%–95%, *n* = 25 boutons). There is a significant difference between the AMPARs PPR and the iGluSnFR PPR in 1 mM $[Ca^{2+}]_e$ (Mann-Whitney test, $p = 0.03$). However, there is no significant difference between the AMPARs PPR and the iGluSnFR PPR in 4 mM $[Ca^{2+}]_e$ (Mann-Whitney test, $p = 0.37$). Value with a PPR = 0 is not plotted for display purpose but was used for statistics. Values are plotted as median with IQR.

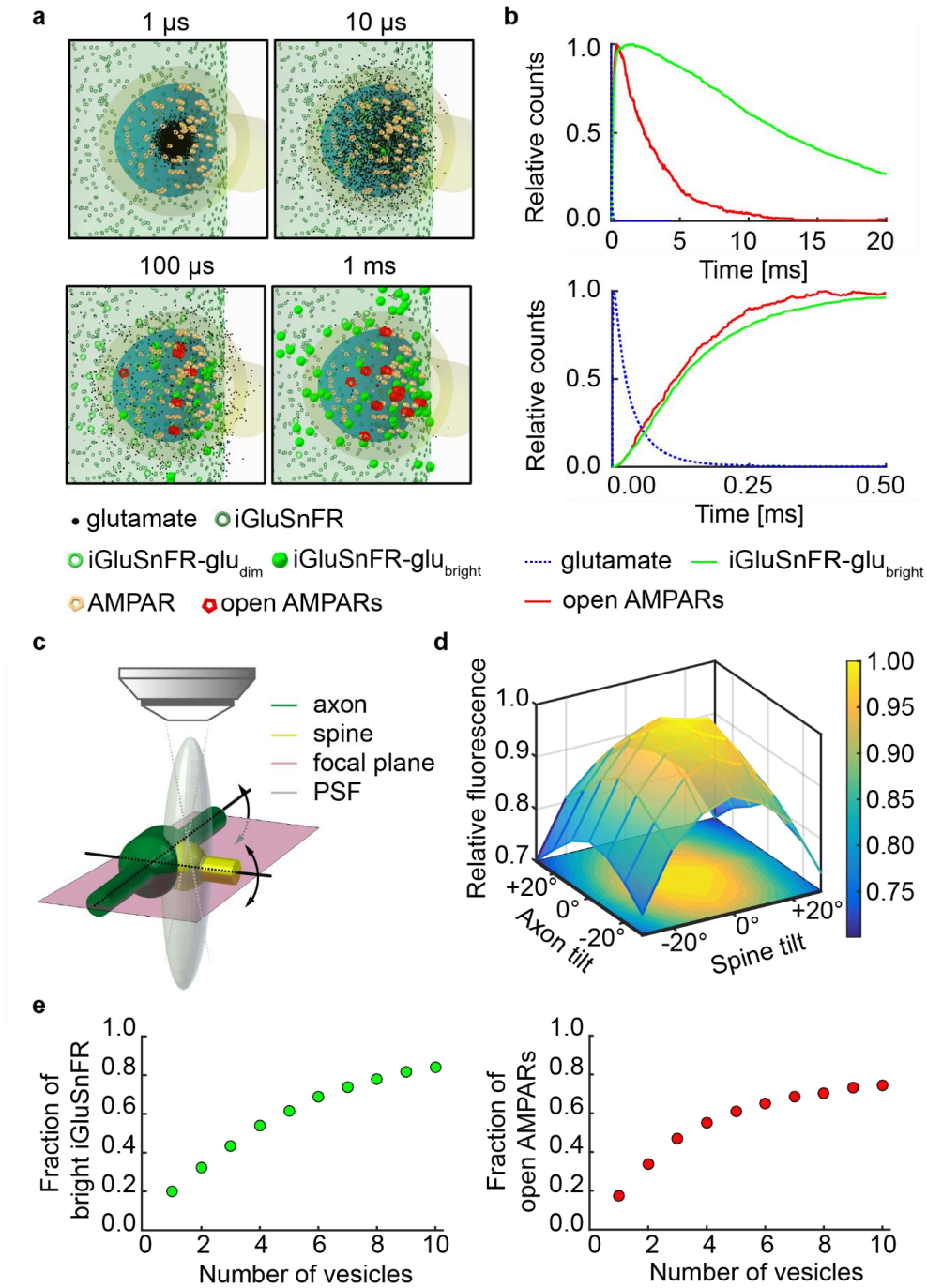

Figure 6: **Monte-Carlo-simulation of glutamate diffusion in the synaptic cleft. a)** Simulated glutamate dynamics within the synaptic cleft upon vesicle release. The model consists of a presynaptic terminal with iGluSnFR molecules opposed to a spine with AMPARs randomly distributed in a disc of 300 nm, separated by a 20 nm synaptic cleft. The synapse is embedded in a network of astrocytes equipped with glutamate transporters. **b)** Simulated reaction time profile of AMPARs opening and iGluSnFR in a bright fluorescent state upon release of a single vesicle containing 3000 molecules of glutamate (*upper panel*) and close-up view of the kinetics from 0 to 50 ms (*lower panel*). **c)** Simulated fluorescence measurements under different orientations of axon and spine with respect to the optical axis. iGluSnFR fluorescence was evaluated inside the PSF. Tilting the axon or the spine reduces $\Delta F/F_0$, as more iGluSnFR molecules outside the synaptic cleft fall within the PSF, contributing to the resting fluorescence F_0. **d)** Normalized fluorescence transient with respect to tilted positions of axon or spine. **e)** Fraction of bright iGluSnFR bound to glutamate (*left panel*) and fraction of open AMPARs (*right panel*) after release of 1-10 vesicles (3000 glutamate molecules per vesicle). Occupancy of iGluSnFR and AMPA receptors is similar after a single vesicle release, resulting in similar saturation curves.

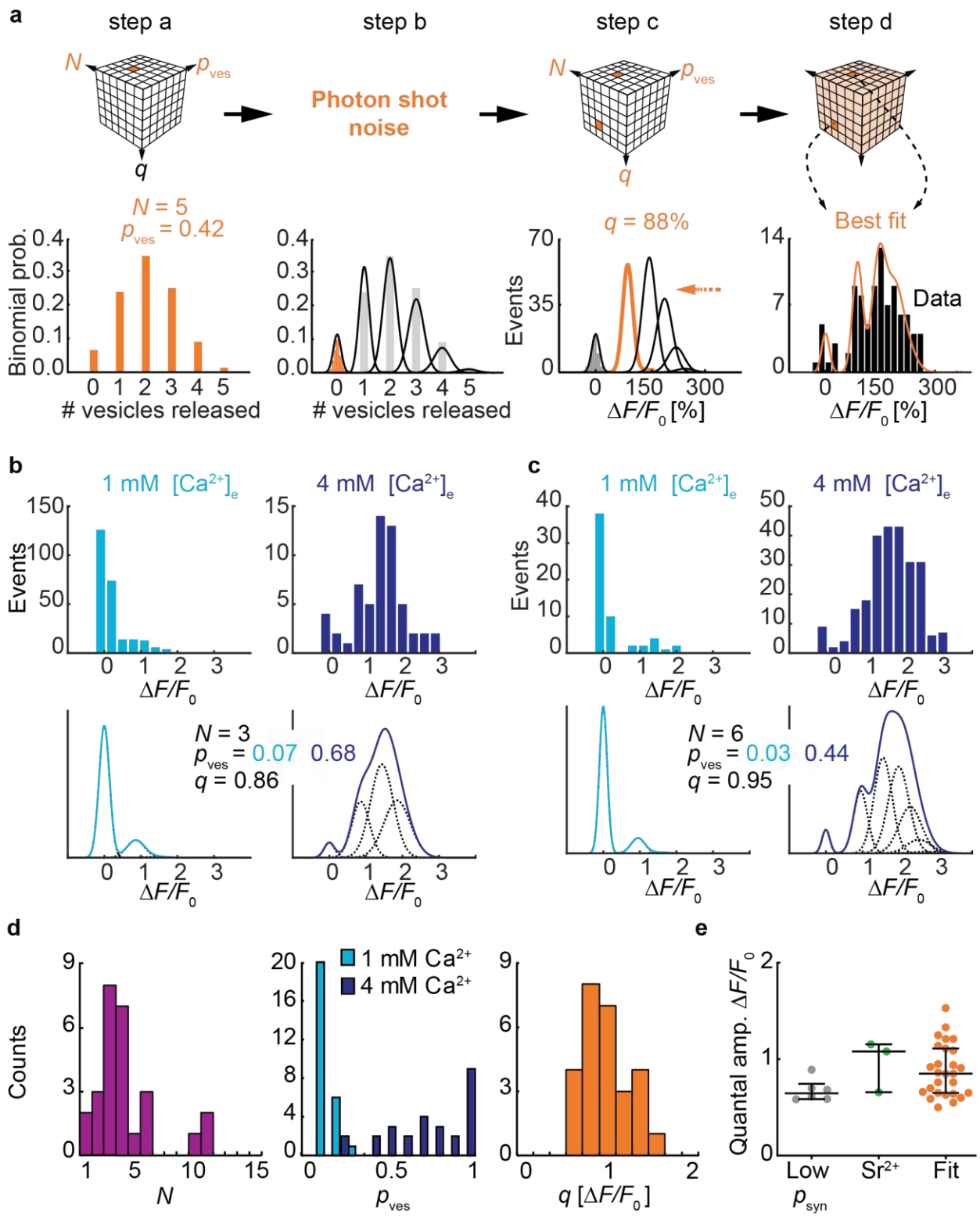

Figure 7: **Extracting *N*, p_{ves} and *q* of Schaffer collateral synapses using a binomial model.** **a)** Schematic view of the exhaustive search of the quantal parameters *N*, p_{ves} and *q*. For a combination of *N* and p_{ves}, the binomial probabilities of the possible outcomes were calculated

(here: N = 5 vesicles and p_{ves} = 0.42). Without stimulation, amplitudes were normally distributed around zero (orange bars). The width of this noise distribution, a function of the number of photons detected from a particular bouton, was used to determine the width of the expected Gaussian probability density functions. A chosen quantal amplitude q (here: 88% $\Delta F/F_0$) sets the spacing of the Gaussian probability density functions. iGluSnFR saturation (max. $\Delta F/F_0$ = 440%) was considered when setting the expected amplitudes of multi-quantal events, leading to a compression (orange arrow) of the individual Gaussians. The resulting probability density function (sum of the Gaussians) was compared to the measured amplitude distribution of a single bouton (black bars, recorded in 2 mM $[Ca^{2+}]_e$). The root mean square (RMS) error was calculated and the best fit (shown here) was selected to determine the synaptic parameters. **b-c)** Single bouton response distributions recorded in 1 mM $[Ca^{2+}]_e$ and 4 mM $[Ca^{2+}]_e$. Two examples from two different slice cultures. The binomial fitting procedure was applied to both histograms, searching for the best combined fit under the condition that N and q had to be identical in 1 mM $[Ca^{2+}]_e$ and 4 mM $[Ca^{2+}]_e$ while p_{ves} could be different. Best fit probability density functions and extracted parameters are shown below the experimental data. **d)** Extracted quantal parameters, N median: 4 vesicles, IQR: 3-5 vesicles; p_{ves} in 1 mM $[Ca^{2+}]_e$ median: 0.07, IQR: 0.03-0.11; p_{ves} in 4 mM $[Ca^{2+}]_e$ median: 0.71, IQR = 0.45-0.96; q median = 0.85 $\Delta F/F_0$, IQR: 0.65-1.11 $\Delta F/F_0$, n = 27 boutons. The numbers delimit the right edge of their respective bin. **e)** Estimating quantal amplitude by three different approaches using independent datasets. Measurements report no significant difference (Kruskal-Wallis test, p = 0.13) between the quantal sizes. p_{syn} < 0.5 boutons in 2 mM $[Ca^{2+}]_e$ median: 0.65 $\Delta F/F_0$, IQR: 0.59-0.75 $\Delta F/F_0$, n = 6 boutons; delayed events in 4 mM $[Sr^{2+}]_e$ wash-in experiments median: 1.08 $\Delta F/F_0$, IQR: 0.66-1.15 $\Delta F/F_0$, n = 3 boutons; binomial fitting procedure median: 0.85 $\Delta F/F_0$, IQR: 0.65-1.11 $\Delta F/F_0$, n = 27 boutons. Values are given as median with IQR.

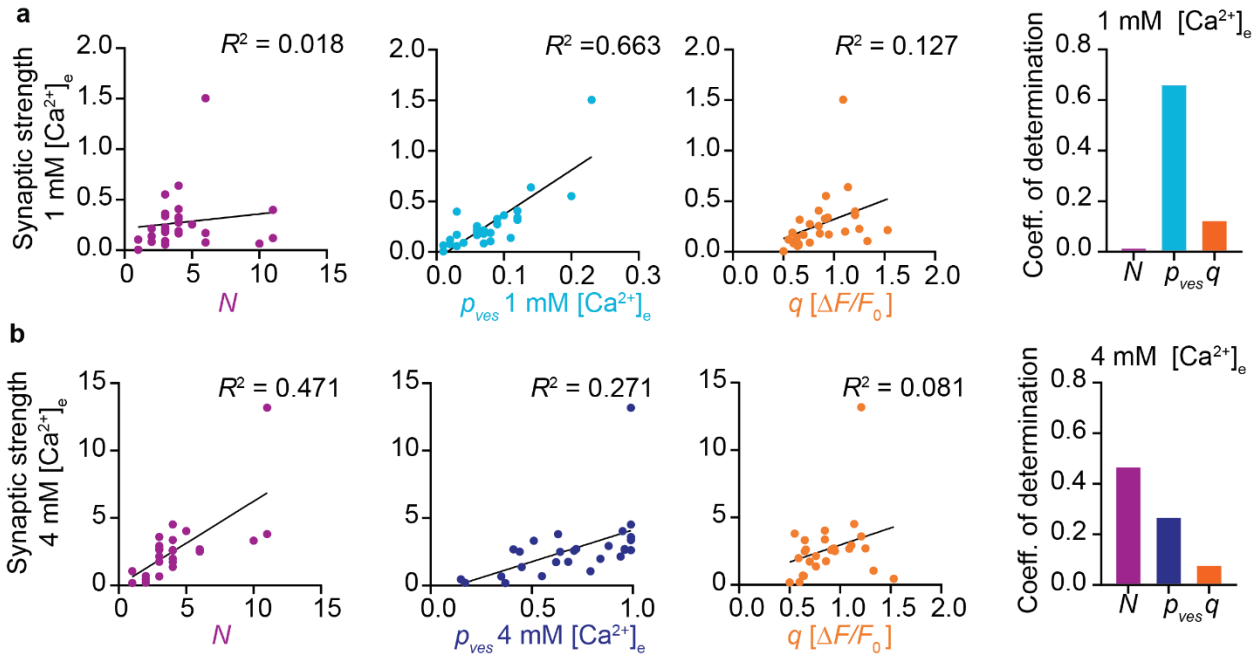

Figure 8**: Quantal parameters and synaptic strength. a)** Correlations between the calculated synaptic strength in 1 mM $[Ca^{2+}]_e$ and the extracted quantal parameters *N*, p_{ves} and *q* (*n* = 27 boutons). **b)** Correlations between the calculated synaptic strength in 4 mM $[Ca^{2+}]_e$ and the extracted quantal parameters *N*, p_{ves} and *q* (*n* = 27 boutons). (First 3 panels) Plot of the calculated synaptic strength in 4 mM $[Ca^{2+}]_e$ from the extracted quantal parameters as shown in Fig. 7 (product of *N*, p_{ves} and *q*) as a function of *N*, p_{ves} 4 mM $[Ca^{2+}]_e$ and *q* (*n* = 27 boutons). (Right panel) summary of the coefficient of determination for the linear correlations between synaptic strength in 4 mM $[Ca^{2+}]_e$ and *N* (R^2 = 0.471), p_{ves} in 1 mM $[Ca^{2+}]_e$ (R^2 = 0.271) and *q* (R^2 = 0.081).

References

1. Del Castillo, J. & Katz, B. Quantal components of the end-plate potential. *J Physiol* **124**, 560–573 (1954).
2. Redman, S. Quantal analysis of synaptic potentials in neurons of the central nervous system. *Physiol. Rev.* **70**, 165–198 (1990).
3. Mainen, Z. F., Malinow, R. & Svoboda, K. Synaptic calcium transients in single spines indicate that NMDA receptors are not saturated. *Nature* **399**, 151–155 (1999).
4. Nimchinsky, E. A., Yasuda, R., Oertner, T. G. & Svoboda, K. The number of glutamate receptors opened by synaptic stimulation in single hippocampal spines. *J Neurosci* **24**,

2054–2064 (2004).

5. Maschi, D. & Klyachko, V. A. Spatiotemporal Regulation of Synaptic Vesicle Fusion Sites in Central Synapses. *Neuron* **94**, 65-73.e3 (2017).

6. Tang, A.-H. *et al.* A trans-synaptic nanocolumn aligns neurotransmitter release to receptors. *Nature* **536**, 210–4 (2016).

7. Rost, B. R. *et al.* Optogenetic acidification of synaptic vesicles and lysosomes. *Nat. Neurosci.* **18**, 1845–1852 (2015).

8. Marvin, J. S. *et al.* An optimized fluorescent probe for visualizing glutamate neurotransmission. *Nat. Methods* **10**, 162–170 (2013).

9. Dürst, C. D. *et al.* High-speed imaging of glutamate release with genetically encoded sensors. *Nat. Protoc.* **14**, 1401–1424 (2019).

10. Jensen, T. P. *et al.* Multiplex imaging relates quantal glutamate release to presynaptic Ca2+ homeostasis at multiple synapses in situ. *Nat. Commun.* **10**, 1414 (2019).

11. Ding, F. *et al.* Changes in the composition of brain interstitial ions control the sleep-wake cycle. *Science (80-.).* **352**, 550–555 (2016).

12. Marvin, J. S. *et al.* Stability, affinity, and chromatic variants of the glutamate sensor iGluSnFR. *Nat. Methods* **15**, 936–939 (2018).

13. Pologruto, T. A., Sabatini, B. L. & Svoboda, K. ScanImage: Flexible software for operating laser scanning microscopes. *Biomed. Eng. Online* **2**, 13 (2003).

14. Christie, J. M. & Jahr, C. E. Multivesicular release at Schaffer collateral-CA1 hippocampal synapses. *J. Neurosci.* **26**, 210–216 (2006).

15. Bolshakov, V. Y., Golan, H., Kandel, E. R. & Siegelbaum, S. A. Recruitment of new sites of synaptic transmission during the cAMP- dependent late phase of LTP at CA3-CA1 synapses in the hippocampus. *Neuron* **19**, 635–651 (1997).

16. Boucher, J., Kröger, H. & Sík, A. Realistic modelling of receptor activation in hippocampal excitatory synapses: Analysis of multivesicular release, release location, temperature and synaptic cross-talk. *Brain Struct. Funct.* **215**, 49–65 (2010).

17. Ricci-Tersenghi, F., Minneci, F., Sola, E., Cherubini, E. & Maggi, L. Multivesicular Release at Developing Schaffer Collateral–CA1 Synapses: An Analytic Approach to Describe Experimental Data. *J. Neurophysiol.* **96**, 15–26 (2006).

18. Oertner, T. G., Sabatini, B. L., Nimchinsky, E. A. & Svoboda, K. Facilitation at single synapses probed with optical quantal analysis. *Nat. Neurosci.* **5**, 657–64 (2002).

19. Tong, G. & Jahr, C. E. Multivesicular release from excitatory synapses of cultered hippocampal neurons. *Neuron* **12**, 51–59 (1994).

20. Rudolph, S., Tsai, M.-C., von Gersdorff, H. & Wadiche, J. I. The ubiquitous nature of multivesicular release. *Trends Neurosci.* **38**, 428–38 (2015).

21. Goda, Y. & Stevens, C. F. Two components of transmitter release at a central synapse. *Proc. Natl. Acad. Sci. U. S. A.* **91**, 12942–12946 (1994).

22. Evans, C. S., Ruhl, D. a. & Chapman, E. R. An Engineered Metal Sensor Tunes the Kinetics of Synaptic Transmission. *J. Neurosci.* **35**, 11769–11779 (2015).

23. Xu-Friedman, M. A. & Regehr, W. G. Probing fundamental aspects of synaptic transmission with strontium. *J. Neurosci.* **20**, 4414–4422 (2000).

24. Blumer, C. *et al.* Automated analysis of spine dynamics on live CA1 pyramidal cells. *Med. Image Anal.* **19**, 87–97 (2015).

25. Rusakov, D. A., Savtchenko, L. P., Zheng, K. & Henley, J. M. Shaping the synaptic signal: Molecular mobility inside and outside the cleft. *Trends Neurosci.* **34**, 359–369 (2011).

26. Jonas, P., Major, G. & Sakmann, B. Quantal components of unitary EPSCs at the mossy fibre synapse on CA3 pyramidal cells of rat hippocampus. *J. Physiol.* **472**, 615–63 (1993).

27. O'Connor, D. H., Wittenberg, G. M. & Wang, S. S.-H. Timing and contributions of pre-synaptic and post-synaptic parameter changes during unitary plasticity events at CA3-CA1 synapses. *Synapse* **61**, 664–678 (2007).

28. Boyd, I. A. & Martin, A. R. The end-plate potential in mammalian muscle. *J. Physiol.* **132**, 74–91 (1956).

29. Debanne, D., Guerineau, N. C., Gahwiler, B. H. & Thompson, S. M. Paired-pulse facilitation and depression at unitary synapses in rat hippocampus: quantal fluctuation affects subsequent release. *J Physiol* **491 (Pt 1**, 163–176 (1996).

30. Emptage, N. J., Reid, C. a, Fine, A. & Bliss, T. V. . Optical Quantal Analysis Reveals a Presynaptic Component of LTP at Hippocampal Schaffer-Associational Synapses. *Neuron* **38**, 797–804 (2003).

31. Yuste, R., Majewska, A., Cash, S. S. & Denk, W. Mechanisms of calcium influx into Hippocampal spines: Heterogeneity among spines, coincidence detection by NMDA receptors, and optical quantal analysis. *J Neurosci* **19**, 1976–1987 (1999).

32. Barbour, B. & Häusser, M. Intersynaptic diffusion of neurotransmitter. *Trends Neurosci.* **20**, 377–384 (1997).

33. Kessler, M., Suzuki, E., Montgomery, K. & Arai, A. C. Physiological significance of high- and low-affinity agonist binding to neuronal and recombinant AMPA receptors. *Neurochem. Int.* **52**, 1383–1393 (2008).

34. Frerking, M. & Wilson, M. Saturation of postsynaptic receptors at central synapses? *Curr. Opin. Neurobiol.* **6**, 395–403 (1996).

35. McAllister, A. K. & Stevens, C. F. Nonsaturation of AMPA and NMDA receptors at hippocampal synapses. *Proc Natl Acad Sci U S A* **97**, 6173–6178 (2000).

36. Scimemi, A. & Beato, M. Determining the neurotransmitter concentration profile at active synapses. *Mol. Neurobiol.* **40**, 289–306 (2009).

37. Armbruster, M., Dulla, C. G. & Diamond, J. S. Effects of fluorescent glutamate indicators on neurotransmitter diffusion and uptake. *Elife* **9**, 1–26 (2020).

38. Siksou, L. *et al.* A common molecular basis for membrane docking and functional priming of synaptic vesicles. *Eur. J. Neurosci.* **30**, 49–56 (2009).

39. Imig, C. *et al.* The Morphological and Molecular Nature of Synaptic Vesicle Priming at Presynaptic Active Zones. *Neuron* **84**, 416–431 (2014).

40. Funahashi, J., Tanaka, H. & Hirano, T. Visualization of Synchronous or Asynchronous Release of Single Synaptic Vesicle in Active-Zone-Like Membrane Formed on Neuroligin-Coated Glass Surface. *Front. Cell. Neurosci.* **12**, 1–10 (2018).

41. Rose, T., Schoenenberger, P., Jezek, K. & Oertner, T. G. Developmental refinement of vesicle cycling at Schaffer collateral synapses. *Neuron* **77**, 1109–21 (2013).

42. Qu, L., Akbergenova, Y., Hu, Y. & Schikorski, T. Synapse-to-synapse variation in mean

synaptic vesicle size and its relationship with synaptic morphology and function. *J. Comp. Neurol.* **514**, 343–352 (2009).

43. Hu, Y., Qu, L. & Schikorski, T. Mean synaptic vesicle size varies among individual excitatory hippocampal synapses. *Synapse* **62**, 953–957 (2008).

44. Soares, C., Trotter, D., Longtin, A., Béïque, J.-C. & Naud, R. Parsing Out the Variability of Transmission at Central Synapses Using Optical Quantal Analysis. *Front. Synaptic Neurosci.* **11**, 22 (2019).

45. James, B., Darnet, L., Moya-Díaz, J., Seibel, S.-H. & Lagnado, L. An amplitude code transmits information at a visual synapse. *Nat. Neurosci.* **22**, 1140–1147 (2019).

46. Sakamoto, H. *et al.* Synaptic weight set by Munc13-1 supramolecular assemblies. *Nat. Neurosci.* **21**, 41–55 (2018).

47. Pulido, C., Trigo, F. F., Llano, I. & Marty, A. Vesicular Release Statistics and Unitary Postsynaptic Current at Single GABAergic Synapses. *Neuron* **85**, 159–172 (2014).

48. Helassa, N. *et al.* Ultrafast glutamate sensors resolve high-frequency release at Schaffer collateral synapses. *Proc. Natl. Acad. Sci.* **115**, 5594–5599 (2018).

49. Gee, C. E., Ohmert, I., Wiegert, J. S. & Oertner, T. G. Preparation of slice cultures from rodent hippocampus. *Cold Spring Harb. Protoc.* **2017**, 126–130 (2017).

50. Wiegert, J. S., Gee, C. E. & Oertner, T. G. Single-cell electroporation of neurons. *Cold Spring Harb. Protoc.* **2017**, 135–138 (2017).

51. Suter, B. A. *et al.* Ephus: multipurpose data acquisition software for neuroscience experiments. *Front. Neural Circuits* **4**, 1–12 (2010).

52. Tigaret, C. M., Tsaneva-Atanasova, K., Collingridge, G. L. & Mellor, J. R. Wavelet transform-based de-noising for two-photon imaging of synaptic Ca2+ transients. *Biophys. J.* **104**, 1006–1017 (2013).

53. Mishchenko, Y. *et al.* Ultrastructural analysis of hippocampal neuropil from the connectomics perspective. *Neuron* **67**, 1009–1020 (2010).

54. Nielsen, T. A., DiGregorio, D. A. & Silver, R. A. Modulation of glutamate mobility reveals the mechanism underlying slow-rising AMPAR EPSCs and the diffusion coefficient in the synaptic cleft. *Neuron* **42**, 757–771 (2004).